THE JOURNAL OF PHYSICAL CHEMISTRY C
A JOURNAL OF THE AMERICAN CHEMICAL SOCIETY

pubs.acs.org/JPCC

Article

Mechanism for the Enhancement of the Oxygen Diffusivity by Cation Substitution in $La_{2-x}Sr_xCuO_4$

Sohee Park, Young-Kyun Kwon,* and Changwon Park*

Cite This: *J. Phys. Chem. C* 2023, 127, 17987−17993

Read Online

ACCESS | Metrics & More | Article Recommendations | Supporting Information

ABSTRACT: Ruddlesden−Popper oxides Ln_2MO_4 (Ln = La, Pr, Nd, Sm; M = Ni, Cu, Fe, Co, Mn) are one of the promising cathode materials for the intermediate temperature (500−750 °C) solid oxide fuel cell. The key property making them operate at relatively low temperatures is their higher oxygen diffusivity, but in general, it is a difficult task to balance it with the durability of the material. To establish guiding principles for systematic improvement, it is indispensable to understand the oxygen diffusion process at the atomic scale. For $La_{2-x}Sr_xCuO_4$, we used density functional theory calculations to identify major diffusion paths and the crucial factors affecting the diffusion of oxygen vacancies. We found that out-of-plane equatorial-to-apical oxygen site hopping is the bottleneck of oxygen diffusion. Sr substitutional doping not only facilitates the formation of oxygen vacancies, i.e., the number of diffusion carriers, but also affects the diffusivity by locally lowering the formation energy. Two competing effects of Sr, weakly trapping the oxygen vacancies and alleviating the bottleneck of the above hopping, are quantified using our realistic random walk simulation, and the resulting diffusion coefficients reveal that the latter dominates at all doping concentrations, but the effect is saturated at $x \sim 0.3$.

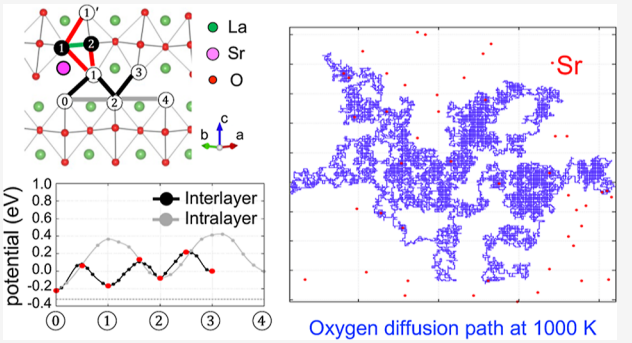

INTRODUCTION

A solid oxide fuel cell (SOFC) is an electrochemical device that produces electricity from oxidizing fuels such as hydrogen, hydrocarbon, or carbon monoxide at solid oxide electrolytes. One of the major challenges in SOFC is lowering the operation temperature to improve its long-term stability and reduce the start-up time of it. In recent years, there have been considerable efforts to search for proper cathode materials, which can operate at the temperature range of 500−750 °C and outperform perovskite-based oxides, such as $La_{1-x}Sr_xCoO_{3-\delta}$,[1] $La_{0.6}Sr_{0.4}Co_{0.2}Fe_{0.8}O_{3-\delta}$,[2] $Ba_{0.5}Sr_{0.5}Co_{0.8}Fe_{0.2}O_{3-\delta}$,[3] $SrNb_{0.1}Co_{0.7}Fe_{0.2}O_{3-\delta}$,[4] and $PrBaCo_2O_{5+\delta}$,[5] which are current choices of commercial use but working at higher temperatures.

It has been recently reported that Ruddlesden−Popper (RP) oxides Ln_2MO_4, in which Ln denotes a lanthanide element such as La, Pr, Nd, or Sm, and M denotes a light late transition metal such as Mn, Mn, Fe, Co, Ni, or Cu, can be promising candidates for the cathode material, due to their fast oxygen reduction reaction kinetics,[6−9] higher oxygen diffusivity than most perovskite-based oxides,[10,11] compatible thermal expansion coefficients with current electrolytes,[12] high chemical stability against oxygen non-stoichiometry,[13] and oxygen partial pressure gradient.[14] Among these properties, their sufficiently high oxygen diffusivity is regarded as a key feature of RP oxides for their intermediate-temperature operation.[15,16] In Ln_2MO_4, oxygen vacancies and interstitials play major roles in oxygen-deficient and oxygen-excessive conditions, respectively,[17] but the underlying atomic processes are usually difficult to identify experimentally. For example, the diffusion paths of an oxygen atom and the effect of cation (Ln) substitution that seems to enhance the oxygen diffusivity[17,18] are still not understood at atomic levels, and complementary calculational approaches are highly desirable.

In this article, using first-principles calculations and diffusion simulations based on the lattice random walk model, we have examined the oxygen vacancy diffusion in oxygen-deficient $La_{2-x}Sr_xCuO_4$. Our calculations clearly show that Sr substitutions for trivalent La not only increase the concentration of oxygen vacancies (diffusion carrier) but also enhance the overall diffusivity by reducing the energy barrier of the bottleneck process in its pristine counterpart.[11]

SIMULATION METHOD

We performed first-principles calculations based on density functional theory as implemented in the Vienna ab initio

Received: May 9, 2023
Revised: August 16, 2023
Published: August 30, 2023

https://doi.org/10.1021/acs.jpcc.3c03072
J. Phys. Chem. C 2023, 127, 17987−17993

simulation package (VASP).[19,20] The electronic wave functions were extended using planewave basis with a kinetic energy cutoff of 400 eV. We employed the spin-polarized generalized gradient approximation with Perdew–Burke–Ernzerhof[21] to treat exchange–correlation functional, and the projector augmented wave method for ionic potentials is adopted.[20] To incorporate the cation substitution and oxygen vacancies, we expanded the primitive unit cell of La_2CuO_4 with lattice constants of $a = b = 5.420$ Å and $c = 13.103$ Å to the $(2\sqrt{2} \times 2\sqrt{2})R45^\circ \times 2$ supercell, which is in the low-temperature tetragonal (LTT) phase, where CuO_6 octahedra are alternately tilted along the [110] direction. It is noted that the pristine La_2CuO_4 is more stable in the low-temperature octahedral phase where the tilting axis is the [100] direction than in the LTT phase.[22,23] It was, however, reported that their energy difference is only ~4.4 meV per formula unit,[22,23] and moreover, a small amount of Sr-substitution reverses such small energy difference, resulting in the LTT to be more stable.[24] The Brillouin zone of the supercell was sampled with a $4 \times 4 \times 1$ k-point mesh. We described the electron correlation associated with the Cu 3d orbital by selecting its on-site Coulomb repulsion[25] to be $U_{eff} \equiv U - J = 7.0$ eV, which reproduces the measured Cu magnetic moment (0.50–0.63 μ_B)[26,27] and band gap (1.80–2.00 eV)[28,29] with 0.603 μ_B and 1.82 eV, respectively. The relative formation energies between different vacancy configurations are substantially less sensitive to the choice of U_{eff}, despite the fact that vacancy formation energy is dependent on U_{eff}, as seen in Figure 1b. Structural optimization was performed until the Hellmann–Feynman forces exerting on each atom in our supercell becomes less than 0.02 eV/Å.

In our diffusion simulations based on the random walk model, we assumed the hopping to path α happens with probability p_α per unit attempt time δt. Here, $p_\alpha \equiv e^{-E_B(\alpha)/k_BT}$ where k_B, T, and $E_B(\alpha)$ are Boltzmann constant, temperature, and energy barrier along path α, respectively. δt is estimated from the harmonic frequency of an oxygen atom around the local minima shown in Figure 2 by fitting second-order polynomials up to the reflection points of the calculated minimum energy paths (MEPs). The calculated δt's are between 0.40 and 0.55 ps, and a common value of 0.5 ps is used for $V_a \Leftrightarrow V_a$, $V_a \leftrightarrow V_a$, and $V_a \leftrightarrow V_e$ hopping. The joint probability $P(\alpha, t)$ for a vacancy to hop along path α at time t is given by

$$P(\alpha, t) = P(t) \times \frac{\overline{p_\alpha}}{\sum_{\alpha=1}^{n} \overline{p_\alpha}} \tag{1}$$

where

$$P(t) = \sum_{\alpha=1}^{n} \left[\overline{p_\alpha} \times \exp\left(-t \sum_{\alpha=1}^{n} \overline{p_\alpha} \right) \right] \tag{2}$$

$\overline{p_\alpha} \equiv \frac{p_\alpha}{\delta t}$, and n is the number of possible hopping paths. The derivations of eqs 1 and 2 can be found in Supporting Information. For a single hopping event, two independent random numbers are generated to sample eq 6, where one is used for determining α and the other is for t.

For a sufficiently long time t, the diffusion coefficient D is calculated from the following relation

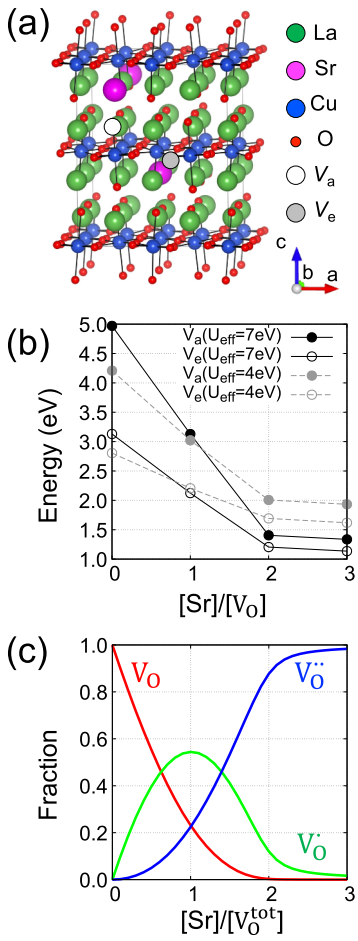

Figure 1. (a) Crystal structure of $La_{2-x}Sr_xCuO_4$. The green, magenta, blue, and red balls represent lanthanum, strontium, copper, and oxygen atoms, respectively. Crystallographic locations of apical (V_a) and equatorial (V_e) vacancies are indicated by white and gray circles. (b) Formation energies of oxygen vacancies for different concentrations of Sr atoms and on-site Coulomb repulsion parameter U_{eff}. [Sr] and [V_O] denote concentrations of Sr atoms and total oxygen vacancies, respectively. (c) Fractions of charge states of oxygen vacancies as a function of Sr concentration at $T = 1000$ K.

$$D = \frac{1}{2n} \frac{\langle r^2 \rangle_t}{t} \tag{3}$$

where n and r^2 are the dimension of the system and the square of displacement, respectively. Bracket means ensemble average over hopping trajectories for large t including over 10,000 hoppings, and 106 trajectories were sampled for the converged values of D.

RESULTS AND DISCUSSION

Stability of Oxygen Vacancies. We explored the relative stability of oxygen vacancies in $La_{2-x}Sr_xCuO_4$ by computing their formation energies. The formation energy depends on their crystallographic locations, charge states, and relative distances from a nearby Sr atom. The oxygen vacancy formation energy, E_V, was calculated using

$$E_V = E_T(La_{2-x}Sr_xCuO_{4-n}) - E_T(La_{2-x}Sr_xCuO_4) + n\mu_O \tag{4}$$

where $E_T(X)$ is the total energy of a system X and μ_O is the chemical potential of an oxygen atom, which was set as half of

https://doi.org/10.1021/acs.jpcc.3c03072
J. Phys. Chem. C 2023, 127, 17987–17993

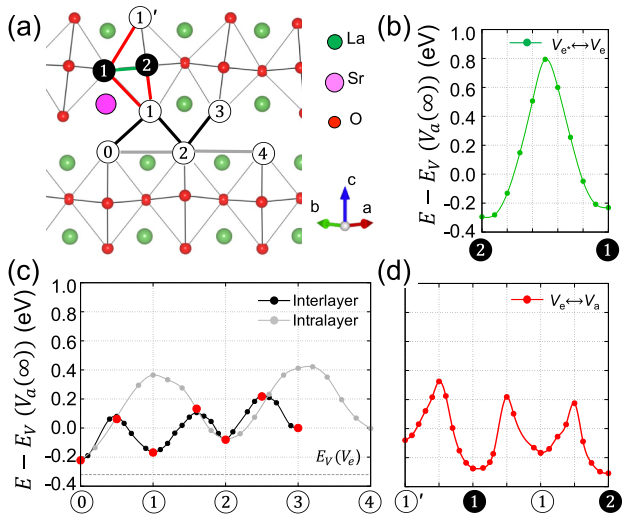

Figure 2. (a) Schematic picture depicting positions of oxygen vacancies and their diffusion paths (thick lines) in $La_{2-x}Sr_xCuO_4$. Oxygen vacant sites are distinguished by their relative position from the nearest Sr atom. MEPs of (b) equatorial-to-equatorial, (c) interlayer (black) and intralayer (gray) apical-to-apical, and (d) apical-to-equatorial hopping are plotted with the corresponding colors of paths in (a). The total energy E of each configuration is plotted relatively with the formation energy of an apical vacancy far from Sr atoms ($E_V(V_a(\infty))$). For comparison, the formation energy of equatorial vacancies is marked with a gray horizontal line in (c).

the total energy of an oxygen molecule O_2 as $\mu_O \equiv \frac{1}{2}E_T(O_2) = -4.892$ eV.

E_V depends both on the crystallographic locations and charge states of the vacancies. As shown in Figure 1a, La_2CuO_4 has a stacked structure of CuO_2 layer (A) and LaO layers (B) repeating as (BAB)(BAB)···, and there are two inequivalent oxygen vacancies at the apical (V_a) and equatorial (V_e) sites of a CuO_6 octahedra. Furthermore, spontaneously tilted CuO_6 octahedra at low temperature[22,23] distinguish their equatorial sites whether they are on the tilt axis or not. We, nevertheless, found that the tilting effect on the vacancy formation at two distinct equatorial sites is quite small; specifically, their formation energy difference is 22 meV in the LTT phase of La_2CuO_4. Hence, we will not distinguish two distinct equatorial vacancies in our vacancy formation analysis hereafter.

The charge states of oxygen vacancies are computationally controlled by replacing La atoms with Sr atoms in a supercell as in $La_{32-n}Sr_nCu_{16}O_{63}$ with $n = 0-3$. When an oxygen vacancy forms, two electrons are released but still weakly bound around the vacancy while a substituted Sr atom attracts one of the electrons and makes the oxygen vacancy be charged.

Figure 1b shows the vacancy formation energy as a function of $n = [Sr]/[V_O]$. In general, V_e has lower formation energy than V_a. As n increases, E_V greatly decreases regardless of the crystallographic location of oxygen vacancy, up to $n = 2$ with which the oxygen vacancy reaches +2 charge state. Further Sr-substitution beyond $n = 2$, however, scarcely changes E_V, indicating that more holes from Sr atoms cannot change the vacancy charge state. Interestingly, the energy difference between V_a and V_e significantly reduces from 1.84 eV for $n = 0$ to 0.20 eV for $n = 2$.[24] This means that when Sr atoms provide sufficient holes, most vacancies become the +2 charge state, letting both V_a and V_e play equally important roles in a diffusion process. To verify the effect of the Hubbard parameter U_{eff}, we also evaluated the vacancy formation energies with $U_{eff} = 4$ and compared them to those with $U_{eff} = 7$ eV. Although the absolute values of the vacancy formation energy are different with U_{eff} values, the relative differences in E_V between V_a and V_e are not so sensitive to the selected U_{eff} value, especially for $n = 2$. As described later, our diffusion simulation only refers to the relative difference in E_V of oxygen vacancies, and thus our results will be robust against the choice of U_{eff}.

In real samples, for a given Sr concentration, three charge states coexist and form a dynamical equilibrium of the following reactions. In the Kröger−Vink notation, these reactions can be written as

$$\begin{cases} V_O + Sr_{La}' + h^\bullet \leftrightarrow V_O^\bullet + Sr_{La}' + \Delta E_1 \\ V_O^\bullet + Sr_{La}' + h^\bullet \leftrightarrow V_O^{\bullet\bullet} + Sr_{La}' + \Delta E_2 \end{cases} \quad (5)$$

The equilibrium concentrations of different charge states were calculated from eqs S4−S7 considering a few conservation relations outlined in Supporting Information. In Figure 1c, the result for $T = 1000$ K with $U_{eff} = 7$ eV are plotted as a function of $n = [Sr]/[V_O]$. In fact, due to the huge energy difference between charge states, the equilibrium concentrations are quite insensitive to T and U_{eff}, and mainly determined by n. As expected, when Sr concentration is larger than twice the oxygen vacancies concentration, most oxygen vacancies become $V_O^\bullet$ and the contributions of higher energy vacancies such as $V_O^{\bullet\bullet}$ or V_O can be neglected for our vacancy diffusion simulation.

Finally, we considered the effect of the Sr environment on E_V. We first checked the presence of any favored Sr configurations in $La_{2-x}Sr_xCuO_4$. Specifically for $La_{30}Sr_2Cu_{16}O_{64}$, we found that E_T varies at most 28 meV depending on the relative position of two Sr atoms within our supercell calculations. Thus, the substituted Sr atoms may be located at any position during a high-temperature synthesis process leading to a random distribution of Sr atoms, which was assumed in our diffusion simulations. More importantly, E_V are reduced when Sr atoms are around them. The details of these effects will be presented in the following diffusion energetics analysis.

We categorized various hopping paths of oxygen vacancies into the following four types: (i) interlayer apical-to-apical hopping ($V_a \Leftrightarrow V_a$), (ii) intralayer apical-to-apical hopping ($V_a \leftrightarrow V_a$), (iii) equatorial-to-equatorial hopping ($V_e \leftrightarrow V_e$), and (iv) apical-to-equatorial hopping ($V_a \leftrightarrow V_e$). Note that the interlayer hopping (i) is denoted by a double arrow. Their respective paths were indicated by black, gray, green, and red/blue arrows in Figure 2a. Note that we are assuming that only oxygen atoms can diffuse through vacancy hoppings and the diffusion through interstitial sites is negligible.

The MEPs provide the atomic picture of the oxygen diffusion processes. From Figure 2, the energy barrier of (i)−(iv) paths are 0.2−0.3, 0.5−0.6, 0.4−0.5, and 1.0−1.1 eV, respectively. Depending on the relative position of the substituted Sr atom, the energy barrier varies by ∼0.1 eV. It is clear that the dominant diffusion paths for the intralayer and interlayer diffusion are $V_a \Leftrightarrow V_a$ and $V_a \leftrightarrow V_e$ hoppings, respectively. If a vacancy is located at an equatorial site, this vacancy can scarcely move directly to another neighboring equatorial site due to the large energy barrier of the $V_e \leftrightarrow V_e$ hopping. Instead, most of them will hop to neighboring apical

https://doi.org/10.1021/acs.jpcc.3c03072
J. Phys. Chem. C 2023, 127, 17987−17993

sites via the $V_e \rightarrow V_a$ hopping. Now, the hopped vacancy at the apical site can move to other apical sites through $V_a \Leftrightarrow V_a$ and $V_a \leftrightarrow V_a$ hopping, or less frequently, move to equatorial sites through the $V_a \leftrightarrow V_e$. Because the $V_a \Leftrightarrow V_a$ hopping is energetically the most favorable, the oxygen diffusion becomes highly anisotropic. As a specific example, in our random walk simulation at 1000 K and small Sr concentration condition ($x < 0.1$), oxygen vacancies spend 70−80% of the time at the equatorial site as being "trapped", and during the rest of the time, the isotropic in-plane oxygen diffusion takes place. So, the major bottleneck of the diffusion process is the escaping process from equatorial sites, i.e., hopping path (iv).

During the diffusion, intriguingly, it was found that the Sr atoms lower E_V of nearby vacancies and tend to weakly bind them around Sr atoms. While at the same time, the Sr atoms help the vacancy to escape from the equatorial sites by lowering E_V of V_a more than that of V_e (which also lowers energy barrier of $V_e \rightarrow V_a$ as will be described in eq 7).

The effect of the substituted Sr atom on E_V of V_a can be described by an effective potential energy $U(c)$ as in

$$E_V(V_a(c)) = E_V(V_a(\infty)) + U_a(c) \quad (6)$$

where c denotes the relative configuration between the Sr atom and V_a and $V_a(\infty)$ is the apical vacancy far from the Sr atoms. $U_a(c)$ is calculated for five configurations indicated as ⓪, ①, ②, ③, and ④ in Figure 2a and becomes saturated as $U_a(***3) \approx U_a(***4) \approx 0$. During our random walk simulation, when two or more Sr atoms are around an apical vacancy site, $U_a(c)$ is calculated for the closest Sr atom.

Similarly, for V_e, we have calculated $U_e(c)$ and found that $U_e(c)$ approached zero at much shorter distance than $U_a(c)$; $U_e(c)$ is −0.066 eV when a Sr atom is in the nearest neighbor of V_e and for farther Sr atoms, $U_e(c)$ is less than 10 meV for our supercell.

Different magnitudes and behaviors of $U_a(c)$ and $U_e(c)$ imply two competing effects of Sr substitutions on oxygen diffusion. One effect is the attraction of vacancies around Sr atoms, which will slow down the diffusion. The other effect is the change of relative formation energy between the apical and equatorial vacancies when the Sr atom is near them. From our calculation, $E_V(V_e(\infty))$ is lower than $E_V(V_a(\infty))$ by 0.293 eV, but it can reduced to ∼0.2 eV with the help of Sr atoms. This also reduces the energy barrier of $V_a \leftrightarrow V_e$ because, to a good approximation, the energy barriers only depend on the relative E_V and hopping paths of two sites from our calculations. As a result, escaping from equatorial sites, which is the bottleneck of the overall diffusion process, becomes more accessible.

To quantify these two competing effects of the Sr atom, we performed random walk simulations on the plausible diffusion paths. In our simulations, the energy barrier E_B from site A to B is calculated as

$$E_B(\mathrm{A} \rightarrow \mathrm{B}) = E_B^0 + \frac{1}{2}\Delta E_V \quad (7)$$

where $\Delta E_V \equiv E_V(\mathrm{B}) - E_V(\mathrm{A})$ is the difference of vacancy formation energy between the two vacancy sites and E_B^0 is 0.256, 0.490, and 0.520 for $V_a \Leftrightarrow V_a$, $V_a \leftrightarrow V_a$, and $V_a \leftrightarrow V_e$, respectively.

Diffusion Kinetics of Vacancies. Figure 3a shows a schematic of oxygen diffusion paths denoted by the solid lines between red balls. The blue balls indicate Cu atoms and La or Sr atoms are not displayed for visual clarity. Note that here we did not consider the $V_e \leftrightarrow V_e$ hopping due to its large energy barrier. The Sr substitutions were randomly placed with the constraint that any two Sr atoms (nearest or next-nearest to each other) were farther apart than the next-nearest neighbor distance between them. As the Sr concentration became higher, this constraint was relaxed to allow two Sr atoms to locate as each other's next-nearest neighbors. The possible hopping paths of V_a (V_e) are 12 (4) and for each path, E_B is assigned by considering its crystallographic location and the Sr environment.

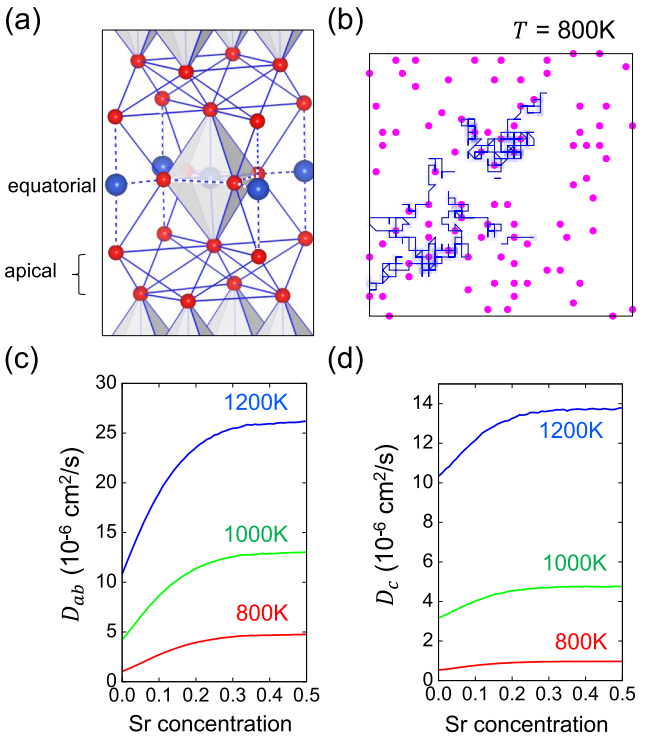

Figure 3. (a) Oxygen diffusion paths (blue lines) in our random walk simulations. Hopping between equatorial sites are not considered due to the high energy barrier. Double layers of apical sites indicated by a red circle form a square lattice when projected in the ab-plane. (b) Typical trajectories of oxygen diffusion (blue solid lines) at double layers of apical sites. Magenta circles denote Sr atoms at the two nearest La planes projected in the ab-plane. Oxygen vacancies stay longer at the sites with darker bluish rectangles. Calculated diffusion coefficients along (c) ab-plane and (d) c-axis as functions of Sr concentration and temperature.

Figure 3b shows the top view of typical trajectories of oxygen vacancies at specific double layers of apical sites at 800 K. Magenta circles denote the location of randomly distributed Sr atoms at the upper and lower planes of the double layer, and $V_a \Leftrightarrow V_a$ ($V_a \leftrightarrow V_a$) hoppings are shown in solid lines parallel (diagonal) to the edge of the square. As expected, oxygen vacancies stay longer around Sr atoms (multiple visits of the same sites are indicated as graded blue colors of rectangles), i.e., weakly bound to Sr atoms. In spite of this behavior, as shown in Figure 3c,d for T = 800, 1000, and 1200 K, respectively, both diffusion coefficients along in-plane (D_{ab}) and out-of-plane direction (D_c) increase as the Sr concentration (x). The increase is larger for D_{ab} and becomes saturated as x increases.

In Figure 4, we quantified the two competing contributions of Sr atoms to oxygen diffusivity, i.e., to weakly bind oxygen vacancy and to help oxygen vacancy escape from the equatorial site. The vacancy diffusion along the in-plane direction

https://doi.org/10.1021/acs.jpcc.3c03072
J. Phys. Chem. C 2023, 127, 17987−17993

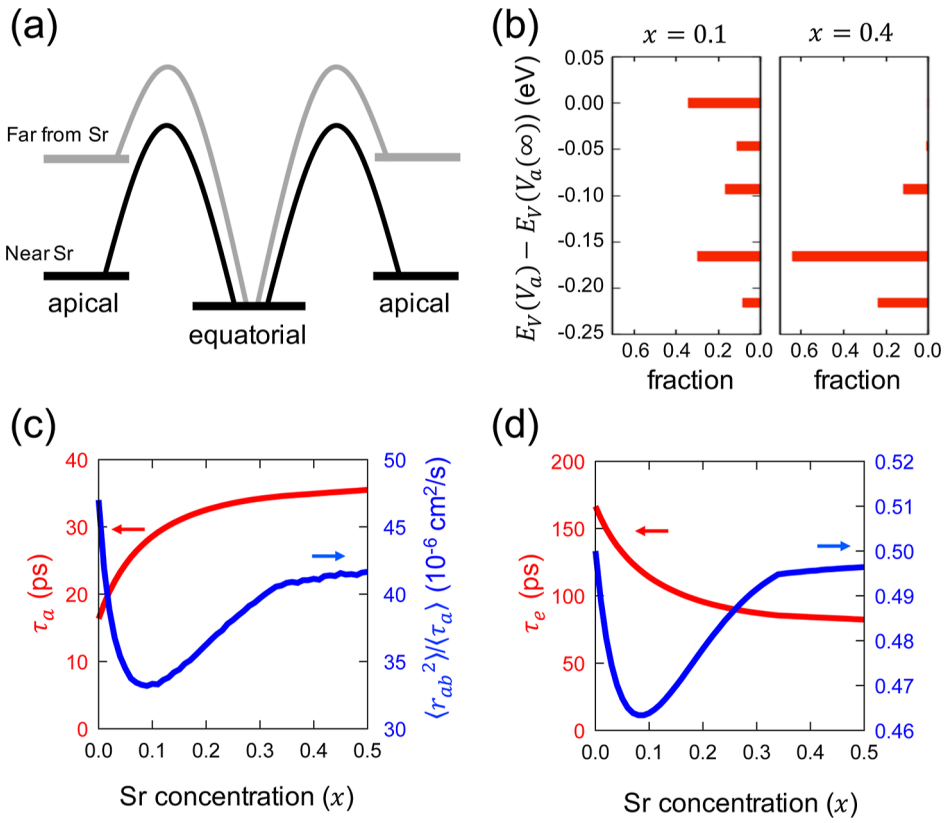

Figure 4. (a) Change of energy barrier for $V_a \leftrightarrow V_e$ hopping when Sr atoms are near. (b) Statistics of $E_V(V_a)$ for Sr concentration (x) in $La_{2-x}Sr_xCuO_4$ is 0.1 (left) and 0.4 (right). (c) Average stay time at apical oxygen planes τ_a (red) and effective in-plane diffusion coefficients (blue) as functions of Sr concentration at T = 1000 K. (d) Average stay time at equatorial sites τ_e (red) and the probability for equatorial vacancies not to hop into the original apical plane they came from (blue).

predominantly occurs at the double layers of apical planes and the diffusion continues until V_a hops into one of the neighboring equatorial sites. If $E_V(V_a)$ is lowered by nearby Sr atoms, V_a can stay longer at the apical planes due to the increase of E_B as shown in Figure 4a. Conversely, the vacancy trapped in the equatorial site can now escape from there more easily because Sr atoms lower the E_B of equatorial-to-apical hopping paths. Statistically, as the Sr concentration increases, the fraction of low-energy apical sites increases, as compared in Figure 4b for x = 0.1 and 0.4. The resulting increase of average stay time at apical (τ_a) and equatorial site (τ_e) is plotted in the red line of Figure 4c,d, respectively for T = 1000 K.

The weakly binding effect of Sr atoms can be resolved in $\langle r_{ab}^2\rangle_{\tau_a}/\tau_a$ where $\langle\rangle_\tau$ indicates average over time τ, which actually measures how well a vacancy diffuse during they are in apical planes. Note that $\langle r_{ab}^2\rangle_{\tau_a+\tau_e} = \langle r_{ab}^2\rangle_{\tau_a}$ and experimentally measured diffusion coefficient is $D_{ab} = \langle r_{ab}^2\rangle_{\tau_a}/(\tau_a + \tau_e)$. In Figure 4c, $\langle r_{ab}^2\rangle/\tau_a$ is plotted as a function of Sr concentration with a blue line. For $x < 0.08$, $\langle r_{ab}^2\rangle/\tau_a$ decreases with increasing x because V_a around Sr atoms tend to be repeatedly attracted to the Sr atom. As x increases further, the attraction ranges of Sr atoms start to overlap and the competing attractions of Sr atoms now reduce the repeating attractions. $\langle r_{ab}^2\rangle/\tau_a$ becomes saturated for $x > 0.3$ when most apical sites become on-sites (⓪) or nearest-neighbors (①) of Sr atoms.

A similar binding effect can also be identified along the out-of-plane direction. If x = 0, the probabilities for V_e to hop into upper and lower apical planes are the same. However, when there is a Sr atom near V_e, V_e favors returning to the original apical plane they came from over the new apical plane without nearby Sr atoms. We quantified this imbalance as f_t which is the probability for V_e to hop into the new apical plane and plotted in Figure 4d as a function of Sr concentration.

In summary, the major bottleneck for the oxygen diffusion in $La_{2-x}Sr_xCuO_4$ is the equatorial-to-apical hopping channel and Sr substitutions relieve it by lowering the formation energy of equatorial vacancies. Though Sr atoms weakly bind oxygen vacancies, which is manifested as the dips of $\langle r_{ab}^2\rangle/\tau_a$ and f_t, the relieving effect greatly surpasses the binding effect that oxygen diffusivity is monotonically enhanced on the concentration of Sr atoms.

CONCLUSIONS

We performed first-principles calculations and diffusion simulations to study oxygen vacancy diffusion in $La_{2-x}Sr_xCuO_4$, and two major hopping channels of the oxygen diffusion are suggested. From the diffusion simulation, it is found that the enhancement by Sr doping is the result of two competing effects; Sr atoms weakly bind oxygen vacancies around themselves, while helping the vacancies to escape from trapping the most stable equatorial sites. It is interesting to compare the intrinsic oxygen diffusivity of $La_{2-x}Sr_xCuO_4$ with that of $La_{2-x}Sr_xNiO_4$ which is another promising candidate material for SOFC where the major carriers of diffusion are interstitial oxygen atoms. According to our calculations, the in-plane energy barriers of oxygen vacancies in $La_{2-x}Sr_xCuO_4$ are between 0.2 and 0.3 eV, while those of oxygen interstitials in

https://doi.org/10.1021/acs.jpcc.3c03072
J. Phys. Chem. C 2023, 127, 17987−17993

$La_{2-x}Sr_xNiO_4$ are between 0.3 and 0.6 eV, depending on the average oxidation states of Ni,[30] i.e., the intrinsic interstitial diffusivity of the latter is several to 10 times lower. As a consequence of the lack of low-energy interstitial sites at CuO_2 planes, one can anticipate that the out-of-plane diffusion of oxygen interstitial is very slow for both $La_{2-x}Sr_xCuO_4$ and $La_{2-x}Sr_xNiO_4$.[31,32] Because the exact vacancy and interstitial concentrations from the proper defect chemistry are not fully understood, the contribution of interstitial oxygens to the oxygen diffusivity in $La_{2-x}Sr_xCuO_4$ at typical operation conditions of SOFC ($p_{O_2} \sim 0.2$ atm, $T \sim 1000$ K) is still unknown. Although there are many interstitial oxygens, their contribution would only be in the in-plane direction, and we believe that this would have little impact on the rate-limiting process (out-of-plane apical to equatorial vacancy hopping) that we have described.

■ ASSOCIATED CONTENT

Supporting Information

The Supporting Information is available free of charge at https://pubs.acs.org/doi/10.1021/acs.jpcc.3c03072.

Derivation of $P(\alpha, t)$ given in eq 1 and evaluation of the equilibrium concentrations of oxygen vacancy charge states (PDF)

■ AUTHOR INFORMATION

Corresponding Authors

Young-Kyun Kwon − *Department of Information Display, Kyung Hee University, Seoul 02447, Korea; Department of Physics and Research Institute for Basic Sciences, Kyung Hee University, Seoul 02447, Korea;* orcid.org/0000-0001-6027-8408; Email: ykkwon@khu.ac.kr

Changwon Park − *School of Computational Sciences, Korea Institute for Advanced Study, Seoul 130-722, Korea;* orcid.org/0000-0002-1788-045X; Email: cwparksnu@gmail.com

Author

Sohee Park − *Department of Information Display, Kyung Hee University, Seoul 02447, Korea*

Complete contact information is available at: https://pubs.acs.org/10.1021/acs.jpcc.3c03072

Notes

The authors declare no competing financial interest.

■ ACKNOWLEDGMENTS

S.H. and Y.K. acknowledge financial support from the Korean government through the National Research Foundation of Korea (NRF-2022R1A2C1005505, NRF-2022M3F3A2A01073562) and the Brain Korea 21 Four Program in 2021. C.P. was supported by the New generation research program (CG079702) at Korea Institute for Advanced Study (KIAS). The computational work was done using the resources of the KISTI Supercomputing Center (KSC-2022-CRE-0062, 2022-CRE-0379) and Center for Advanced Computation of KIAS.

■ REFERENCES

(1) Tsvetkov, N.; Lu, Q.; Sun, L.; Crumlin, E. J.; Yildiz, B. Improved chemical and electrochemical stability of perovskite oxides with less reducible cations at the surface. *Nat. Mater.* **2016**, *15*, 1010−1016.

(2) Januschewsky, J.; Ahrens, M.; Opitz, A.; Kubel, F.; Fleig, J. Optimized $La_{0.6}Sr_{0.4}CoO_{3-\delta}$ Thin-Film Electrodes with Extremely Fast Oxygen-Reduction Kinetics. *Adv. Funct. Mater.* **2009**, *19*, 3151−3156.

(3) Shao, Z.; Haile, S. M. A high-performance cathode for the next generation of solid-oxide fuel cells. *Nature* **2004**, *431*, 170−173.

(4) Zhou, W.; Sunarso, J.; Zhao, M.; Liang, F.; Klande, T.; Feldhoff, A. A Highly Active Perovskite Electrode for the Oxygen Reduction Reaction Below 600 °C. *Angew. Chem., Int. Ed.* **2013**, *52*, 14036−14040.

(5) Chen, D.; Ran, R.; Shao, Z. Assessment of $PrBaCo_2O_{5+\delta}$-$Sm_{0.2}Ce_{0.8}O_{1.9}$ composites prepared by physical mixing as electrodes of solid oxide fuel cells. *J. Power Sources* **2010**, *195*, 7187−7195.

(6) Li, Q.; Zhao, H.; Huo, L.; Sun, L.; Cheng, X.; Grenier, J.-C. Electrode properties of Sr doped La_2CuO_4 as new cathode material for intermediate-temperature SOFCs. *Electrochem. Commun.* **2007**, *9*, 1508−1512.

(7) Zheng, K.; Gorzkowska-Sobaś, A.; Świerczek, K. Evaluation of Ln_2CuO_4 (Ln: La, Pr, Nd) oxides as cathode materials for IT-SOFCs. *Mater. Res. Bull.* **2012**, *47*, 4089−4095.

(8) Caronna, T.; Fontana, F.; Natali Sora, I.; Pelosato, R.; Viganò, L. Chemical compatibility of Sr-doped La_2CuO_4 cathode material with LSGM solid oxide electrolyte. *Solid State Ionics* **2010**, *181*, 1355−1358.

(9) Kolchina, L.; Lyskov, N.; Pestrikov, P.; Istomin, S.; Mazo, G.; Antipov, E. Evaluation of $La_{1.8-x}Pr_xSr_{0.2}CuO_{4-\delta}$ oxides as cathode materials for IT-SOFCs. *Mater. Chem. Phys.* **2015**, *165*, 91−96.

(10) Skinner, S.; Kilner, J. Oxygen diffusion and surface exchange in $La_{2-x}Sr_xNiO_{4+\delta}$. *Solid State Ionics* **2000**, *135*, 709−712.

(11) Boehm, E.; Bassat, J.-M.; Dordor, P.; Mauvy, F.; Grenier, J.-C.; Stevens, P. Oxygen diffusion and transport properties in non-stoichiometric $Ln_{2-x}NiO_{4+\delta}$ oxides. *Solid State Ionics* **2005**, *176*, 2717−2725.

(12) Ding, X.; Kong, X.; Wang, X.; Jiang, J.; Cui, C. Characterization and optimization of $Ln_{1.7}Sr_{0.3}CuO_4$ (Ln=La, Nd)-based cathodes for intermediate temperature solid oxide fuel cells. *J. Alloys Compd.* **2010**, *502*, 472−476.

(13) Meyer, T. L.; Jacobs, R.; Lee, D.; Jiang, L.; Freeland, J. W.; Sohn, C.; Egami, T.; Morgan, D.; Lee, H. N. Strain control of oxygen kinetics in the Ruddlesden-Popper oxide $La_{1.85}Sr_{0.15}CuO_4$. *Nat. Commun.* **2018**, *9*, 92.

(14) Al Daroukh, M.; Vashook, V.; Ullmann, H.; Tietz, F.; Arual Raj, I. Oxides of the AMO_3 and A_2MO_4-type: structural stability, electrical conductivity and thermal expansion. *Solid State Ionics* **2003**, *158*, 141−150.

(15) Brett, D. J.; Atkinson, A.; Brandon, N. P.; Skinner, S. J. Intermediate temperature solid oxide fuel cells. *Chem. Soc. Rev.* **2008**, *37*, 1568−1578.

(16) Shao, Z.; Tadé, M. O. Intermediate-temperature solid oxide fuel cells. *Chem. Soc. Rev.* **2016**, *37*, 1568.

(17) Lee, D.; Lee, H. N. Controlling Oxygen Mobility in Ruddlesden−Popper Oxides. *Materials* **2017**, *10*, 368.

(18) Li, L.; Zhou, J.; Hu, Z.; Choi, S.; Kim, G.; Wang, J.-Q.; Zhang, L. First-Principles Insight into the Effects of Intrinsic Oxygen Defects on Proton Conduction in Ruddlesden−Popper Oxides. *J. Phys. Chem. Lett.* **2021**, *12*, 11503−11510.

(19) Kohn, W.; Sham, L. J. Self-Consistent Equations Including Exchange and Correlation Effects. *Phys. Rev.* **1965**, *140*, A1133−A1138.

(20) Kresse, G.; Joubert, D. From ultrasoft pseudopotentials to the projector augmented-wave method. *Phys. Rev. B: Condens. Matter Mater. Phys.* **1999**, *59*, 1758−1775.

(21) Perdew, J. P.; Burke, K.; Ernzerhof, M. Generalized Gradient Approximation Made Simple. *Phys. Rev. Lett.* **1996**, *77*, 3865−3868.

(22) Furness, J. W.; Zhang, Y.; Lane, C.; Buda, I. G.; Barbiellini, B.; Markiewicz, R. S.; Bansil, A.; Sun, J. An accurate first-principles treatment of doping-dependent electronic structure of high-temperature cuprate superconductors. *Commun. Phys.* **2018**, *1*, 11.

(23) Lee, C.-C.; Chiu, J.-Y.; Yamada-Takamura, Y.; Ozaki, T. Hidden competing phase revealed by first-principles calculations of phonon instability in the nearly optimally doped cuprate La1.875Sr0.125CuO4. *Phys. Rev. B* **2021**, *104*, 064114.
(24) Park, S.; Kwon, Y.-K.; Yoon, M.; Park, C. Role of Sr doping and external strain on relieving bottleneck of oxygen diffusion in $La_{2-x}Sr_xCuO_{4-\delta}$. *Sci. Rep.* **2022**, *12*, 13378.
(25) Hubbard, J. Electron correlations in narrow energy bands. *Proc. R. Soc. London, Ser. A* **1963**, *276*, 238−257.
(26) Yamada, K.; Kudo, E.; Endoh, Y.; Hidaka, Y.; Oda, M.; Suzuki, M.; Murakami, T. The effect of the heat treatments on the antiferromagnetism in $La_2CuO_{4-\delta}$ single crystals. *Solid State Commun.* **1987**, *64*, 753−756.
(27) Vaknin, D.; Sinha, S.; Moncton, D.; Johnston, D.; Newsam, J.; Safinya, C.; King, H., Jr Antiferromagnetism in La_2CuO_{4-y}. *Phys. Rev. Lett.* **1987**, *58*, 2802−2805.
(28) Ginder, J.; Roe, M.; Song, Y.; McCall, R.; Gaines, J.; Ehrenfreund, E.; Epstein, A. Photoexcitations in La_2CuO_4: 2-eV energy gap and long-lived defect states. *Phys. Rev. B: Condens. Matter Mater. Phys.* **1988**, *37*, 7506−7509.
(29) Cooper, S.; Thomas, G.; Millis, A.; Sulewski, P.; Orenstein, J.; Rapkine, D.; Cheong, S.; Trevor, P. Optical studies of gap, exchange, and hopping energies in the insulating cuprates. *Phys. Rev. B: Condens. Matter Mater. Phys.* **1990**, *42*, 10785−10788.
(30) Xu, S.; Jacobs, R.; Morgan, D. Factors Controlling Oxygen Interstitial Diffusion in the Ruddlesden−Popper Oxide $La_{2-x}Sr_xNiO_{4+\delta}$. *Chem. Mater.* **2018**, *30*, 7166−7177.
(31) Jorgensen, J.; Dabrowski, B.; Pei, S.; Richards, D.; Hinks, D. Structure of the interstitial oxygen defect in $La_2NiO_{4+\delta}$. *Phys. Rev. B: Condens. Matter Mater. Phys.* **1989**, *40*, 2187−2199.
(32) Paulus, W.; Cousson, A.; Dhalenne, G.; Berthon, J.; Revcolevschi, A.; Hosoya, S.; Treutmann, W.; Heger, G.; Le Toquin, R. Neutron diffraction studies of stoichiometric and oxygen intercalated La_2NiO_4 single crystals. *Solid State Sci.* **2002**, *4*, 565−573.

https://doi.org/10.1021/acs.jpcc.3c03072
J. Phys. Chem. C 2023, 127, 17987−17993